IEEE Robotics and Automation Letters (RA-L) paper, presented at ICRA 2026, Vienna, Austria. Cite as RA-L paper.

TIPS: Tiered Information-Rich Planning Strategy for Efficient AGV Autonomous Exploration

Zhuoxuan Wang, *Graduate Student Member, IEEE*, Shuguo Pan, Jinle Xu, *Student Member, IEEE*, Xianlu Tao, Wang Gao, and Qiang Wang

***Abstract*—In this letter, we propose a tiered systematic framework to enhance the overall efficiency and environmental coverage of autonomous exploration for Autonomous Ground Vehicle (AGV) in complex environments with narrow regions.At the local level, we introduce a novel Multi-cause Triggering Sensor Model (MTSM) to improve informative observation acquisition in narrow regions. Furthermore, the Frontier set is defined from a probabilistic distribution perspective and utilized to optimize the initial training pool of Bayesian optimization, thereby accelerating convergence toward the optimal navigation target point. At the global level, we incrementally maintain an Information-Rich Sparse Roadmap (IRSR) by leveraging accumulated historical exploration knowledge. When a dead zone situation is detected, the heuristic guidance is activated and realized by graph search considering information content and distance between IRSR vertices, enabling AGV to maintain a continuous and sustained exploration process. Three simulation scenarios with increasing complexity are designed, in which comprehensive comparisons and evaluations against different types of state-of-the-art approaches are conducted. The results demonstrate that our framework achieves a favorable balance between algorithm runtime, exploration efficiency and coverage completeness, with superior performance in narrow regions. Subsequent real-world experiments further validate the strong potential of our proposed method for practical applications.**

***Index Terms*—Autonomous agents, path planning, probability density function.**

I. Introduction

In RECENT years, autonomous exploration with autonomous ground vehicles (AGVs) has attracted growing attention due to its potential in various fields that human cannot directly set foot in, e.g., scene reconstruction, resource exploration, and underground navigation. Thus far, numerous advanced exploration planning methodologies have been proposed for enhancing the exploration efficiency and environmental information acquisition throughout the process [1], [2], [3]. Yet, some common challenges remain inadequately addressed.

One major issue is the greedy strategy and the absence of global guidance, which often result in redundant paths and the exploration trapped into a dead zone [4], [5]. As a result, the AGV spends excessive time moving through explored areas, increasing energy consumption and hindering overall exploration performance. On the other hand, some advanced exploration methods prioritize efficiency but struggle with narrow regions (i.e., narrow passages, compact rooms and small corners), or even ignore them altogether, adversely impacting exploration coverage and success rates [6], [7]. Therefore, it is important to endow exploration planning methods with the capability to efficiently and rapidly collect environmental information while achieve high coverage rate.

Motivated by these facts, a novel **T**iered **I**nformation-rich **P**lanning **S**trategy (TIPS) is proposed in this letter for fast and efficient AGV exploration, which encompasses two pivotal components: a local plan for accurate environmental information acquisition and exploration optimization, and a global plan for dead zone escape and heuristic guidance. At the local planning level, we design a novel cause-triggered sensor model to enhance information acquisition and more accurately describe the environment, especially in narrow regions (Section IV-A). Then, the Frontier set is defined from a probabilistic distribution perspective and the optimal target is determined using Bayesian Kernel Inference and Optimization (BKIO) [7], where we refine the initial training pool through Frontiers for fast convergence (Section IV-B). At the global planning level, we maintain a lightweight topology roadmap, where key vertices are retained in information-rich areas (Section IV-C). When a dead zone situation is detected, global planning is activated and achieved through graph search, effectively guiding the AGV to escape and resume exploration (Section IV-D). The proposed framework is compared with state-of-the-art methods in multiple simulation scenarios, and validated in a real-world indoor environment (Section V). The main contributions of this letter are summarized as:

1) A Multi-cause Triggering Sensor Model (MTSM) that provides enhanced environment representation, especially in narrow areas. The Frontier set is defined from a probabilistic distribution perspective and used for BKIO initial training pool, enabling faster optimal target determination.
2) An Information-Rich Sparse Roadmap (IRSR) that retains suboptimal Frontiers during exploration. A 2-opt method with Christofides optimized initial solution is developed

Received 21 June 2025; accepted 15 October 2025. Date of publication 22 October 2025; date of current version 3 November 2025. This article was recommended for publication by Associate Editor S. Santra and Editor A. Banerjee upon evaluation of the reviewers' comments. This work was supported in part by the Frontier Technology R&D Program Project of Jiangsu Province under Grant BF2024009, in part by the Postgraduate Research & Practice Innovation Program of Jiangsu Province under Grant KYCX25_0438, and in part by the Science and Technology Project of State Grid Corporation of China under Grant J2024159. *(Corresponding author: Shuguo Pan.)*

Zhuoxuan Wang, Shuguo Pan, Jinle Xu, Xianlu Tao, and Wang Gao are with the School of Instrument Science and Engineering, State Key Laboratory of comprehensive PNT Network and Equipment Technology, Southeast University, Nanjing 210096, China (e-mail: wangzhuoxuan@seu.edu.cn; psg@seu.edu.cn; xujinle@seu.edu.cn; xltao@seu.edu.cn; gaow@seu.edu.cn).

Qiang Wang is with the College of Automation & College of AI, Nanjing University of Posts and Telecommunications, Nanjing 210023, China (e-mail: wangqiang@njupt.edu.cn).

This article has supplementary downloadable material available at https://doi.org/10.1109/LRA.2025.3623934, provided by the authors.

Digital Object Identifier 10.1109/LRA.2025.3623934

2377-3766 © 2025 IEEE. All rights reserved, including rights for text and data mining, and training of artificial intelligence and similar technologies. Personal use is permitted, but republication/redistribution requires IEEE permission. See https://www.ieee.org/publications/rights/index.html for more information.

©2026 IEEE

Authorized licensed use limited to: Southeast University. Downloaded on November 04,2025 at 02:29:11 UTC from IEEE Xplore. Restrictions apply.

IEEE Robotics and Automation Letters (RA-L) paper, presented at ICRA 2026, Vienna, Austria. Cite as RA-L paper.

to solve a graph-based optimization problem, providing heuristic global guidance path in dead zones and ensuring continuous, sustained exploration process.

3) Extensive simulations and real-world experiments, demonstrating the superior performance of our method in runtime, exploration efficiency and environment coverage. The code will be open source to benefit the community[1].

II. Related Work

The most common methods for solving AGV autonomous exploration problem rely on Frontier-based or sampling-based approaches [5]. More recently, many studies have formulated autonomous exploration as a process of reducing environmental uncertainty, putting information theory as a new perspective for solving exploration problems.

The Frontier-based method was first proposed by Yamauchi [8], defining the Frontier as the boundary between known and unknown spaces, and selecting one Frontier as the navigation target. Building upon this pioneering work, numerous studies have been laid out for improvement [2], [3], [6], [9], [10]. [9] defined exploration subregions and introduced a hybrid Frontier filtering method at the point cloud level to reduce algorithmic complexity. [10] proposed a Frontier information structure and a three-stage planning strategy for global coverage. Despite these seminal works, Frontier-based methods still encounter notable challenges—Frontier clustering is time consuming and the myopic greedy strategies often lead to inefficient back-and-forth movements.

Sampling-based methods gained attention with the Next Best View Planner (NBVP) [11], which employed Rapidly Random Trees (RRT) for sampling and executed the first segment of branch with the highest gain. Since then, various sampling-based approaches have emerged [1], [4], [12], [13], [14]. [1] used uniform sampling and constrained Dijkstra's search range by motion cost to accelerate path search toward the point with the highest gain. [12] improved the NBVP framework by biasing sampling toward areas of interest, and reusing visited nodes to avoid tree reconstruction. Nevertheless, these methods still suffer from low exploration efficiency, particularly in narrow areas where node sampling is difficult, and maintaining the tree structure requires significant computational resources as the environment expands.

Information gain-based approaches enable holistic environmental quantification and evaluation by leveraging entropy and mutual information (MI) theory. They are considered a promising strategy for balancing exploration efficiency and completeness [15], thus overcoming the limitations of greedy strategies in Frontier-based series and randomness inherent in sampling-based methods [16]. However, existing approaches still face two major limitations. First, sensor models used to update map belief are often unsatisfactory, especially in narrow regions. Many methods rely on the naive Inverse Sensor Model (ISM) to update voxel occupancy [17], [18], [19], which use Log-odds that may cause abrupt changes in parameter, diminishing the contribution of accumulated observational data to MI and ignoring the environment structural information. Consequently, voxel occupancy updates can be incomplete and inaccurate. Some works, e.g., [20] and [21] adopt the Sensor Cause Model (SCM) as an alternative, which uses the estimated occupancy of each voxel on the beam to achieve a gradual transition of parameters. However, SCM performs poorly in narrow regions as it only considers forward ray propagation, with occupancy updates dependent on ray length. In such cases, the ray propagation distance is much shorter than the sensor maximum range, limiting the update of voxel occupancy and resulting in only modest reduction in map entropy, even though the sensor's field of view (FoV) is already sufficient to cover the entire environment. Second, evaluating the total information gain of the environment imposes substantial computational overhead on edge computing devices, making real-time computation infeasible [16]. Although prior studies have employed statistical techniques to mitigate computational cost by training minor parts of samples to approximate the whole, e.g., Gaussian Process with Bayesian Optimization (GPBO) in [22] and Bayesian Kernel Inference and Optimization (BKIO) in [7], they often overlook the impact of initial sample quality on iterative optimization, which may compromise robust real-time performance.

In contrast, the proposed tiered framework addresses the limitations of existing information gain-based methods in both environmental information acquisition in narrow regions and computational efficiency through a novel sensor model at the local level. In addition, it provides global heuristic guidance for dead zone scenarios, which are often neglected in previous studies, thereby enabling a continuous and sustained exploration process. Consequently, the AGV achieves fast, efficient, and complete environment coverage.

III. Preliminaries

A. Occupancy Grid Map

In this letter, we use a 2D occupancy grid map (2D-OGM) m for environment representation given the condition of relatively stable change in elevation, fulfilling the AGV operating criteria. Yet, we need to clarify that our method is not inherently restricted to 2D conditions and can be readily extended to 3D scenarios.

Definition 1 (Occupancy State): Each voxel m^k_{bin} in the OGM is binary that can be either *Occupied* ($m^k_{bin} = 1$) or *Free* ($m^k_{bin} = 0$), and $p(m^k_{bin} = 0) = 1 - p(m^k_{bin} = 1)$. The occupancy states of voxels are independent of one another.

Definition 2 (Continuous Observation OGM): Rather than directly storing the binary occupancy state $m^k_{bin} \in \{0, 1\}$ for each voxel, the map maintains a continuous occupancy state $m^k \in [0, 1]$ derived from the marginal probability density function (state belief) $b^{m^k}_t = p(m^k | \mathcal{Z}_{0:t}, \mathcal{X}_{0:t})$ [20], where $\mathcal{Z}_{0:t}$ and $\mathcal{X}_{0,t}$ are historical observations $\mathcal{Z}$ and sensor configurations $\mathcal{X}$ from 0 to t. $p(m^k)$ is used to represent the probability of *Occupied* and meets the following equation:

$$p(m^k) = \mathbb{E}(m^k) = \hat{m}^k = \int_0^1 m^k b^{m^k}_t dm^k \tag{1}$$

Each unobserved voxel is assumed uniform with $p(m^k) = 0.5$. Since the OGM is incrementally constructed from observations and voxel occupancy state is continuous, we define the map as a **Continuous Observation OGM** and denote it by $\tilde{m}$. In addition, we preserve the premise of voxel independence but consider the observation interdependence between voxels in our method. As a result, the Markov assumption inherent in traditional Log-odds method [17] is eliminated, enabling full use of historical exploration data while preserving the environment structural description [23].

[1]The code will be open source at https://github.com/WangZX-SEU/TIPS

Authorized licensed use limited to: Southeast University. Downloaded on November 04,2025 at 02:29:11 UTC from IEEE Xplore. Restrictions apply.

IEEE Robotics and Automation Letters (RA-L) paper, presented at ICRA 2026, Vienna, Austria. Cite as RA-L paper.

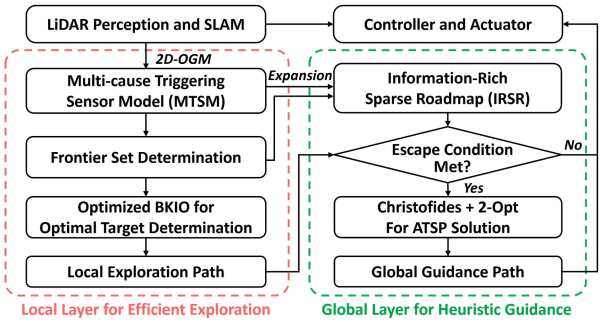

Fig. 1. The flow chart of the proposed framework.

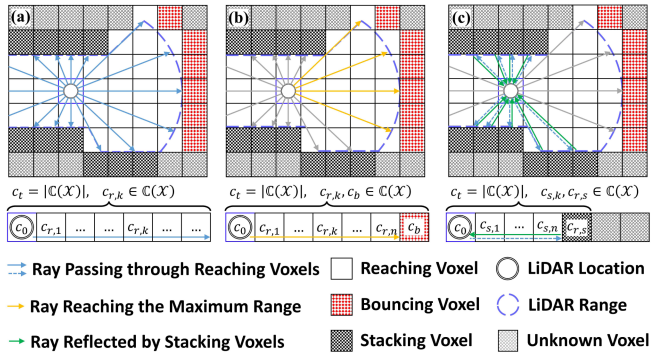

Fig. 2. An illustration of MTSM in an FoV with multiple rays. (a) Rays pass Reaching voxels, $\mathrm{Tc}(R)$ is triggered. (b) Rays reach Bouncing voxels at the maximum distance z_{max}, $\mathrm{Tc}(R)$ and $\mathrm{Tc}(B)$ are triggered. (c) Rays reflected by Stacking voxels, $\mathrm{Tc}(R)$, $\mathrm{Tc}(B)$ and $\mathrm{Tc}(S)$, are triggered. .

B. Entropy and Information Gain

Information gain-based exploration strategy aims to minimum environment uncertainty through change of voxel entropy $\mathbb{H}(\cdot)$ in OGM before and after observed by the sensor, which is defined as the Mutual Information (MI) $\mathbb{I}(\cdot)$:

$$\begin{aligned}&\mathbb{I}(\tilde{m} \mid \mathcal{Z}_t, \mathcal{Z}_{0:t-1}, \mathcal{X}_{0:t-1}) \\ &\quad = \mathbb{H}[p(\tilde{m} \mid \mathcal{Z}_{0:t-1}, \mathcal{X}_{0:t-1}] - \mathbb{H}[p(\tilde{m} \mid \mathcal{Z}_t, \mathcal{Z}_{0:t-1}, \mathcal{X}_{0:t-1})]\end{aligned} \tag{2}$$

where t is the current planning period, $\mathcal{Z}_t$ is the new observation data. Shannon Entropy (SE) is the most widely accepted form for measuring uncertainty [21]:

$$\begin{aligned}\mathbb{H}_{SE}[p(\tilde{m})] = &-\sum_{k=1}^{n} p(\tilde{m}^k) \log\left[p(\tilde{m}^k)\right] \\ &+ (1 - p(\tilde{m}^k)) \log\left[(1 - p(\tilde{m}^k))\right]\end{aligned} \tag{3}$$

The entropy of a voxel is maximized when it is totally unknown ($p(m^k) = 0.5$), and attains the minimum when the occupancy state is fully determined ($p(m^k) = 0$ or 1).

Consider the beam-based sensor equipped by the AGV is composed of several independent narrow beams with a finite range, and the perceptual field consists of voxels that intersect with these beams. Then, drawing upon the definition of MI, the information gain of a voxel can be formally given:

Definition 3 (Information Gain): When the sensor is positioned at $\tilde{m}^k$, the information gain is defined as the sum of MI of the voxels across all independent beams:

$$\mathbb{I}(\tilde{m}^k) = \sum_{i=0}^{n_b} \mathbb{I}\left(\tilde{m}^{[i]}; \mathcal{I}_k^{[i]}\right) = \sum_{i=0}^{n_b} \sum_{j=0}^{n_z} \mathbb{I}\left(\tilde{m}_j^{[i]}; \mathcal{I}_k^{[i]}\right) \tag{4}$$

where $\mathcal{I}_k$ denotes the beam set at $\tilde{m}^k$, n_b, n_z are quantities of beams and voxels along each respective beam, $\tilde{m}^{[i]}$ refers to the set of voxels intersected with $\mathcal{I}_k^{[i]}$.

IV. Tiered Information-Rich Planning Strategy

The overall flow chart of the framework is illustrated in Fig. 1. The LiDAR-based SLAM inputs the 2D-OGM into the framework. At the local layer, an improved sensor model is employed to update the belief of the local environment and to partition the Frontier set. An optimized BKIO method is then used to rapidly determine the optimal target, enabling efficient local exploration. At the global layer, the remaining voxels and Frontiers are utilized to maintain a sparse roadmap. Once the escape condition is satisfied, a global path planning is solved to provide heuristic guidance and ensure the continuity of exploration.

A. Multi-Cause Triggering Sensor Model

Here, we consider the AGV equips with a LiDAR characterized by a maximum sensing range of $z_{\max}$. As assumed in III-B, the FoV is modeled as a set of measurement cones $\mathbb{C} = Cone(\mathcal{X})$, where each cone is assumed to consist of sufficiently narrow rays intersected with voxels emitted from the LiDAR, as shown in Fig. 2. Customarily, the Bayesian Inference (BI) is used for map occupancy state update as:

$$\begin{aligned}&p(\tilde{m}^k|\mathcal{Z}_t, \mathcal{Z}_{0:t-1}, \mathcal{X}_{0:t}) = \\ &\quad \eta^{-1} p(\mathcal{Z}_t|\tilde{m}^k, \mathcal{Z}_{0:t-1}, \mathcal{X}_{0:t})\, p(\tilde{m}^k|\mathcal{Z}_{0:t-1}, \mathcal{X}_{0:t-1})\end{aligned} \tag{5}$$

where η is the normalization factor. $p(\mathcal{Z}_t)$ is the *Forward Sensor Model* used as a likelihood function to quantify the confidence in depth measurements [20]. $p(\tilde{m}^k|\mathcal{Z}_{0:t-1}, \mathcal{X}_{0:t-1})$ is the prior distribution, usually implemented via ISM or SCM.

As we mentioned in Section IV-A, the Log-odds update of ISM and the principle of SCM both limit the comprehensiveness of environmental information acquisition in narrow regions. To address this issue, we propose a novel Multi-cause Triggering Sensor Model (MTSM) in this letter, which considers *Reaching*, *Bouncing*, and notably *Stacking* causes to determine the probability distribution of ray reflection at all possible voxels $c \in \mathbb{C}(\mathcal{X})$, $c_t = |C(\mathcal{X})|$ under map uncertainty, as depicted in Fig. 2. In particular, if a ray reflects before reaching z_{max}, the information content of voxels in the corresponding region is increased. This enhancement enables a more realistic estimation of entropy variation and a more accurate environment representation, especially in narrow regions. MTSM can be written as:

$$\begin{aligned}&p(c_{r,k}|b_{t-1}^{\tilde{m}}, \mathcal{X}_t) = \mathcal{M}_k = \mathrm{Tc}(S^{c_{r|s,0:n}}, B^{c_{r,b}}, R^{c_{r,0:n}}|b_{t-1}^{\tilde{m}}, \mathcal{X}_t) \\ &= \underbrace{\mathrm{Tc}(S^{c_{r|s,0:n}}|B^{c_{r,b}}, R^{c_{r,0:n}}, b_{t-1}^{\tilde{m}}, \mathcal{X}_t)}_{\text{Stacking cause}} \\ &\quad \times \underbrace{\mathrm{Tc}(B^{c_{r,b}}|R^{c_{r,0:n}}, b_{t-1}^{\tilde{m}}, \mathcal{X}_t)}_{\text{Bouncing cause}} \underbrace{\mathrm{Tc}(R^{c_{r,0:n}}|b_{t-1}^{\tilde{m}}, \mathcal{X}_t)}_{\text{Reaching cause}}\end{aligned} \tag{6}$$

where $\mathcal{X}_t$ denotes the ray at t-th time step. Tc abbreviates *Triggering Cause*, which can be interpreted as a binary switch that

Authorized licensed use limited to: Southeast University. Downloaded on November 04,2025 at 02:29:11 UTC from IEEE Xplore. Restrictions apply.

IEEE Robotics and Automation Letters (RA-L) paper, presented at ICRA 2026, Vienna, Austria. Cite as RA-L paper.

activates the corresponding term in Eq.(6) only when the cause meets the specified conditions described below. Meanwhile, the triggering order in Eq.(6) is fixed as $\mathrm{Tc}(R)$, $\mathrm{Tc}(B)$, and $\mathrm{Tc}(S)$, and each triggered term is left-multiplied by the previous one.

The first cause $\mathrm{Tc}(R)$ triggers when the ray can pass through all previous voxels before k-th. The *Reaching* cause voxels are drawn in black hollow squares in Fig. 2, whose expression is:

$$\begin{aligned}\mathrm{Tc}(R^{c_{r,0:n}}|b_{t-1}^{\tilde{m}},\mathcal{X}_t) &= \prod_{k=0}^{n}\left(1-\mathrm{Tc}(B_r^{c_k}|R^{c_{r,0:k-1}},b_{t-1}^{\tilde{m}},\mathcal{X}_t)\right)\\ &= \prod_{k=0}^{n}(1-\hat{m}^{c_{r,k}}) \end{aligned} \tag{7}$$

When the ray reaches the maximum range z_{max}, the second cause $\mathrm{Tc}(B)$ is triggered as defined in Eq.(8). At this point, the ray can pass through all the voxels before c_b and stop. It is important to note that c_b is set as the last voxel of the $\mathbb{C}(\mathcal{X})$. The *Bouncing* cause voxel are drawn in red checkerboard squares in Fig. 2.

$$\begin{aligned}\mathrm{Tc}(B^{c_{r,b}}|R^{c_{r,0:n}},b_{t-1}^{\tilde{m}},\mathcal{X}_t) &= E(\hat{m}^{c_{r,b}}) = \hat{m}^{c_{r,b}}\\ &= \int_0^1 \hat{m}^{c_{r,b}} p(\hat{m}^{c_{r,b}}|z_{0:t-1},x_{0:t-1})d\hat{m}^{c_{r,b}}\end{aligned} \tag{8}$$

Finally, but most importantly, if the ray encounters an obstacle and triggers $\mathrm{Tc}(B)$ at $c_{r,s}$ before reaching z_{max}, i.e., the ray length $d_{r,s} < z_{max}$, the third cause $\mathrm{Tc}(S)$ will be activated. The primary purpose of the *Stacking* cause is to artificially increase the information feedback obtained by the LiDAR, thereby enhancing the confidence in the belief update of narrow regions. $\mathrm{Tc}(S)$ is supposed to be directly related to $d_{r,s}$, with a stronger influence when the stacking voxel $c_{r,s}$ is closer to the LiDAR. By doing so, the entropy of narrow regions can be effectively reduced. The *Stacking* cause voxels are drawn in black grid squares in Fig. 2. $\mathrm{Tc}(S)$ is designed as follows:

$$\begin{aligned}\mathrm{Tc}(S^{c_{r|s,0:n}}|B^{c_{r,b}},R^{c_{r,0:n}},b_{t-1}^{\tilde{m}},\mathcal{X}_t) &= \rho\cdot\mathrm{Tc}(R_t^{c_{s,0:n}}|b_{t-1}^{\tilde{m}})\\ &= \rho\cdot\mathrm{Tc}(R_t^{c_{r,0:m}}|b_{t-1}^{\tilde{m}}) = \rho\cdot\prod_{k=0}^{n}(1-\hat{m}^{c_{s,k}})\end{aligned} \tag{9}$$

where $\rho = \frac{\alpha}{d_{r,s}}$ is a scaling factor and only effective when $d_{r,s} < z_{\max}$. The constant part of ρ is set to $\alpha \in (1,\infty)$, as the influence of the *Stacking* cause decreases with increasing distance from the current AGV location. Combining Eq.(6) $\sim$ (9), Eq.(5) can be modified when three causes are triggered as:

$$\begin{aligned}p(c_t|\mathcal{Z}_t,\mathcal{Z}_{0:t-1},\mathcal{X}_{0:t}) &= \eta^{-1}\cdot p(\mathcal{Z}_t|c_t,b_{t-1}^{\tilde{m}},\mathcal{X}_t)\\ &\times\rho\cdot\hat{m}^{c_{r,s}}\prod_{i=0}^{k}(1-\hat{m}^{c_{r,i}})\prod_{i=0}^{k}(1-\hat{m}^{c_{s,i}})\end{aligned} \tag{10}$$

Consequently, the state belief of the k-th voxel can be updated in Eq.(11) using Eq.(6) and Eq.(5), which is then incorporated into Eq.(1) to compute the expected occupancy.

$$\begin{aligned}b_t^{\tilde{m}^k} &= \sum_{c_{r,k}\in\mathbb{C}} p(\tilde{m}^k|c_{r,k},\mathcal{Z}_{0:t},\mathcal{X}_{0:t})\cdot p(c_{r,k}|\mathcal{Z}_t,\mathcal{Z}_{0:t-1},\mathcal{X}_{0:t})\\ &= \sum_{c_{r,k}\in\mathbb{C}} \frac{p(c_{r,k}|\tilde{m}^k,b_{t-1}^{\tilde{m}^k},\mathcal{X}_t)}{p(c_{r,k}|b_{t-1}^{\tilde{m}^k},\mathcal{X}_t)}\cdot p(c_{r,k}|b_{t-1}^{\tilde{m}^k},\mathcal{Z}_t,\mathcal{X}_t)\cdot b_{t-1}^{\tilde{m}^k}\end{aligned}$$

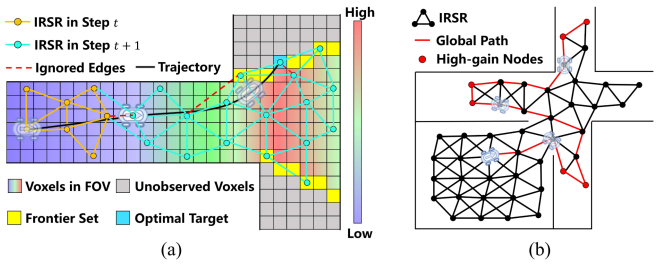

Fig. 3. Schematic of IRSR. (a) Optimal target determination and expansion of IRSR. The heatmap represents the amount of information contained in each voxel. (b) Heuristic global guidance based on IRSR. .

$$= \begin{cases}\frac{\tilde{m}^k+\hat{m}^k}{\hat{m}^k}\mathcal{M}_k b_{t-1}^{\tilde{m}^k} & ,\text{if } !\mathrm{Tc}(S)\\ \frac{\tilde{m}^k+\hat{m}^k}{\hat{m}^k}\mathcal{M}_k b_{t-1}^{\tilde{m}^k}+\frac{1-\tilde{m}^k}{1-\hat{m}^k}\sum_{i=k+1}^{n}\mathcal{M}_i, & \text{if } \mathrm{Tc}(S)\end{cases} \tag{11}$$

B. Optimal Target Determination

The AGV performs high-resolution omnidirectional raycasting every time it moves, and then updates the map belief through Eq.(5) $\sim$ (11). Following this, the optimal target for the next movement needs to be determined. However, it is mentioned in [6] that the time consumption of this determina- tion process can account for up to 95% of the entire planning time, making the calculation of all voxels' information gain within FoV impractical. To address this, we adopt an online supervised learning method based on Bayesian Kernel Inference Optimization (BKIO) proposed in [7]. It estimates the information gain of querying samples $\mathbf{x}^*$ with length ℓ from a sequence of explicitly evaluated samples $\mathbf{x}$ that satisfy the Gaussian Process assumption, and employs Bayesian Optimization to provide an asymptotically optimal solution, thereby reducing the computational cost.

$$\bar{\mathbf{y}}^* = \mathbb{E}[\mathbf{y}^*|\mathbf{x}^*,\mathcal{Q}] \approx \frac{\bar{\mathbf{y}}}{\bar{k}},\quad \sigma(\mathbf{y}^*) = \mathrm{Var}[\mathbf{y}^*|\mathbf{x}^*,\mathcal{Q}] \approx \frac{\sigma(\mathbf{x}^*)}{\bar{k}}$$

$$\bar{\mathbf{y}} = \sum_{i=1}^{\ell} k(\mathbf{x}^*,\mathbf{x})\mathbf{y}_i,\qquad \bar{k} = \sum_{i=1}^{\ell} k(\mathbf{x}^*,\mathbf{x}) \tag{12}$$

where $k(\mathbf{x}^*,\mathbf{x})$ is the Matérn $5/2$ kernel, $\mathcal{Q} = \{\mathbf{x}_i,\mathbf{y}_i \mid i = 0,\ldots,l\}$ is the initial training pool. $\mathbf{x}_i = (x_i, y_i, \theta_i, \mathrm{idx}_i, \mathrm{idy}_i)$ is the sample state including coordinates, heading angle, and indices. $\mathbf{y}_i = \mathbb{I}(\tilde{m}^i)$ is defined as the expected information gain evaluated by omnidirectional *virtual* raycasting on $\tilde{m}$ at $\mathbf{x}_i$ [7]. $\mathbf{y}^*$ is the estimated information gain. $\bar{\mathbf{y}}^*$ is the posterior mean. $\sigma(\mathbf{x}^*)$ and $\sigma(\mathbf{y}^*)$ are covariance matrices.

Notably, BKIO does not screen the initial samples in $\mathcal{Q}$, while it is essential to extract more information from the environment when the quantity of training pool is small [24]. To address this issue, we adopt the concept of Frontier in this letter to form an optimized initial training pool. Since the occupancy probability of voxels in OGM is uniformly initialized to 0.5, which can be considered completely "unknown", and the corresponding value will be updated through MTSM after observation. Then, the Frontier can be defined from the probabilistic distribution perspective as voxels adjacent to those with an occupancy probability of 0.5:

$$\begin{aligned}\mathcal{F} &= \{\tilde{m}_f \in \mathrm{FoV} \mid p(\tilde{m}_f) \neq 0.5 \text{ and } \exists\,\mathcal{N}(\tilde{m}_f) = 0.5\}\\ \mathcal{N}(\tilde{m}_f) &= \{(\mathrm{idx}_f-1,\mathrm{idy}_f),(\mathrm{idx}_f+1,\mathrm{idy}_f),\end{aligned}$$

Authorized licensed use limited to: Southeast University. Downloaded on November 04,2025 at 02:29:11 UTC from IEEE Xplore. Restrictions apply.

IEEE Robotics and Automation Letters (RA-L) paper, presented at ICRA 2026, Vienna, Austria. Cite as RA-L paper.

Algorithm 1: Local planning of TIPS.

Require: 2D-OGM $\tilde{m}$, Map entropy $\mathbb{H}[p(\tilde{m})]$, State belief $b^{\tilde{m}}_{t-1}$ at time $t-1$, Current observation $\mathcal{Z}_t$, Current state $\mathbf{x}_{cur}$, Max optimization epoch N_{epoch}, Frontier set $\mathcal{F}$

if exploration continue **and** not global planning **then**
  $\mathcal{F} = \{\tilde{m}_f \in \text{FoV} | p(\tilde{m}_f) \neq 0.5 \,\&\, \exists \mathcal{N}(\tilde{m}_f) = 0.5\}$;
  $\mathcal{Q} \leftarrow \{\mathbf{x}_j, \mathbf{y}_j \mid \mathbf{x}_j \in \mathcal{F}, j = 0, .., l\}$;
  for $\mathbf{x}_i$ in $\mathcal{Q}$ **do**
    $\mathcal{X}_t \leftarrow$ **OmnidirectionalVirtualRaycasting**$(\mathbf{x}_i, \tilde{m})$;
    $\mathcal{M} \leftarrow$ **ComputeMTSM**$(\tilde{m}, b^{\tilde{m}}_{t-1}\mathcal{Z}_t, \mathcal{X}_t)$;
    $b^{\tilde{m}^{\mathbf{x}_j}}_{t-1} \leftarrow$ **CalStateBelief**$(\mathcal{M}, b^{\tilde{m}}_{t-1}\mathcal{Z}_t, \mathcal{X}_t)$;
    $\mathbb{H}[p(\hat{m}^{\mathbf{x}_j})] \leftarrow$ **CalEntropy**$(\hat{m}, \alpha, b^{\tilde{m}^{\mathbf{x}_j}}_{t-1})$;
    $\mathbf{y}_j = \mathbb{I}[p(\hat{m}^{\mathbf{x}_j})] = \mathbb{H}[p(\tilde{m}^{\mathbf{x}_j})] - \mathbb{H}[p(\hat{m}^{\mathbf{x}_j})]$;
  end for
  iter $= 0$; // *BKIO for optimal target determination*
  for iter $<$ N_{epoch} **do**
    iter $=$ iter $+ 1$;
    $\{\mathbf{x_o}, \mathbf{y_o}, \text{idx}\} \leftarrow$ **BKIOptimization**$(\mathcal{Q}, \mathcal{F})$;
    $\mathbf{x}$ **in** $\mathcal{Q}$? $\mathcal{Q} \leftarrow \mathcal{Q} \bigcup (\mathbf{x_o}, \mathbf{y_o})$: $\mathbf{y}(\text{idx}) \leftarrow \mathbf{y_o}$
  end for
  $\mathcal{L}_{local} \leftarrow$ **Astar**$(\mathbf{x}_{cur}, \mathbf{x}_o)$
end if
return $\mathcal{L}_{local}$

$$(\text{idx}_f, \text{idy}_f), (\text{idx}_f, \text{idy}_f + 1)\} \tag{13}$$

$$\mathcal{Q} = \{\mathbf{x}_j, \mathbf{y}_j \mid \mathbf{x}_j \in \mathcal{F}, j = 0, .., l\} \tag{14}$$

Herein, idx_f, idy_f are indices of Frontiers in OGM. From Eq.(4), it is known that Frontiers are voxels exhibits higher expected information gain $\mathbf{y}_i$, i.e., holds greater potential to guide the AGV toward unknown regions. Thus, the initial training pool can be constructed from the Frontier set, as defined in Eq.(14). This approach facilitates faster convergence of the BO process and reduces randomness during the initial optimization stage. Given the initial training pool, the information gain corresponding to $\mathbf{x}^*$ can be directly queried via Eq.(12).

Ultimately, $\mathbf{x}_o$ with the highest utility is selected using the *Distance-based Upper Confidence Bound (DUCB)* function [24] in BKIO process (Eq.(15)), where a Euclidean distance cost d is considered to avoid excessive energy consumption. κ is a trade-off factor for balancing Exploration and Exploitation. In this way, the target point can be guided to favor Frontier regions, while without overly prioritizing information richness and leading to a greedy strategy. The BKIO is iterated until convergence or the maximum iteration is reached. The final output $\mathbf{x}_o$ is the optimal target, highlighted by the blue box in Fig. 3, and the information-rich exploration path $\mathcal{L}_{local}$ can be extracted using A$*$ algorithm. The belief of OGM and the corresponding occupancy are continuously updated when the AGV navigates along the $\mathcal{L}_{local}$, until a new frame of perceptual information is received and the re-planning procedure is triggered. The whole local planning process can be found in Algorithm1.

$$\mathbf{x}_o = \arg\max_{\mathbf{x} \in \mathcal{Q}} \quad \bar{\mathbf{y}} + \kappa\sigma(\mathbf{y}) + \gamma d(\mathbf{x}, \mathbf{x}_{cur}) \tag{15}$$

C. Information-Rich Sparse Roadmap

The AGV exploration process is inevitably faced with dead zones, which are considered in this work under the following conditions: (1) The heading angle changes drastically within four steps; (2) The change of $\mathbb{I}(\tilde{m})$ is less than a predefined threshold when moving towards the optimal target; (3) The Frontier set $\mathcal{F}$ is empty. In such cases, the reuse of the local planning strategy may cause back-and-forth maneuvers and significant resource overhead. Therefore, integrating the accumulated knowledge from the exploration process to guide the AGV escape dead zones is critical to improve overall exploration efficiency. In this letter, we maintain a sparse roadmap to achieve fast and heuristic escape path searching. Specifically, the roadmap is an "Information-Rich" (IRSR) undirected graph $\mathbf{G}_I = (\mathbf{V}, \mathbf{E} | \{\mathbf{x}, \mathbf{y}\} \in \mathbf{V}, \{d\} \in \mathbf{E})$, where $\{\cdot\}$ represents the attribute contained by edge $\mathbf{E}$ or vertex $\mathbf{V}$.

After determining $\mathbf{x}_o$, the AGV current state $\mathbf{x}_{cur}$ is first added to the graph. Suboptimal Frontiers in $\mathcal{F}$ are sorted in descending order of $\mathbf{y}$ and considered as the candidate vertex set $\mathbf{V}_1$, while other voxels within the known area are sorted in ascending order of distance to $\mathbf{x}_{cur}$ and formed as the candidate vertex set $\mathbf{V}_2$. Then, nodes in $\mathbf{V}_2$ are sequentially evaluated for the connection condition to $\mathbf{G}_I$, that is, whether the minimum distance is greater than r and the collision checking is satisfied. Those that pass the evaluation are added to $\mathbf{G}_I$. Once $\mathbf{V}_2$ is empty, the same evaluation process is applied to $\mathbf{V}_1$. Moreover, to ensure sparsity, the distance between vertices in $\mathbf{G}_I$ must also exceed r. Ultimately, the roadmap retains high information-gain Frontier voxels and ensures accessible paths for the AGV to reach them. The expansion process of IRSR is shown in Fig. 3.

As the exploration advances, the value of $\mathbf{y}$ at vertices in IRSR within explored areas will decrease with the update of the map belief by MTSM. Consequently, the retained high-gain nodes correspond to regions like intersections or doorways that have significant information gain in multiple directions, as shown in Fig. 3(b) with red nodes.

D. Dead Zone Escape and Global Guidance

The global planning is activated when the exploration is deemed to be in dead zones, which is a path optimization method in TIPS that considers both information gain and movement distance to solve an Asymmetric Traveling Salesman Problem (ATSP), aiming at providing heuristic global guidance to help the AGV escape dead zones and resume the exploration process in high-gain regions.

$$\begin{aligned} \mathcal{S} &\sim \{s_\zeta = \mathbf{y}_\zeta \cdot \mathbf{D}(v_\zeta) \mid \mathrm{v}_\zeta \in \mathbf{G}_I(\mathbf{V}),\ \mathbf{y}_\zeta > \mathbb{I}_{thr}\} \\ \mathbf{D}(v_\zeta) &= \exp(-\lambda \mathbf{L}(\mathbf{x}_{cur}, \mathrm{v}_\zeta)), \quad ||\mathcal{S}|| = n \end{aligned} \tag{16}$$

Herein, $\mathcal{S}$ represents the set of scores s of $\mathbf{v}$ in IRSR whose information gain is beyond the threshold $\mathbb{I}_{thr}$, with the length of n. $\mathbf{D}$ is the penalty function, where $\mathbf{L}$ denotes the total movement distance from $\mathbf{x}_{cur}$ to $\mathbf{v}_\zeta$ through edges in $\mathbf{G}_I$.

The scores in $\mathcal{S}$ are used to construct the cost matrix $\mathbf{M}_{atsp} \in \mathbb{R}^{(n+1)\times(n+1)}$, with the first column set to zero. Finally, the open-loop traversal path can be obtained using 2-opt search [6]. Specifically, the Christofides algorithm is applied to optimize the initial path, with a theoretical approximation guarantee of no more than 1.5 times the optimal solution, thereby reducing iteration times and enhancing path quality. The global planning is illustrated in Fig. 3(b) with red lines.

V. Experimental Evaluation

The proposed framework is verified in this section through simulation and real-world environments. The simulated and real AGVs are based on Scout mini platform as shown in Fig. 8. All

Authorized licensed use limited to: Southeast University. Downloaded on November 04,2025 at 02:29:11 UTC from IEEE Xplore. Restrictions apply.

IEEE Robotics and Automation Letters (RA-L) paper, presented at ICRA 2026, Vienna, Austria. Cite as RA-L paper.

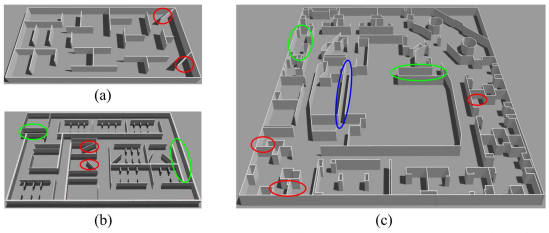

Fig. 4. Simulation environments. Partial narrow regions are enclosed in the figure, with small corners, compact rooms, and narrow passages marked by red, green, and blue ovals, respectively. (a) Maze. (b) Indoor. (c) Lab.

TABLE I
EXPERIMENT CONFIGURATIONS

	2D-OGM		Local Layer		Global Layer		Others	
Parameter	Resolution	Inflate	κ	γ	r	n	Velocity	z_{max}
Value	0.4m	0.2m	5	0.5	1.5m	10	2m/s	10m

TABLE II
STATISTIC RESULTS OF TEST 1 OVER 10 RUNS

Scene / Size(m) / Max entropy[1] (bits)	Method	Exploration time(s)↓*		Algorithm runtime[2](ms)↓		Entropy change(bits)↑		Coverage rate[3](%)↑
		Avg	*Std*	*Avg*	*Std*	*Avg*	*Std*	*Avg*
Maze 35×24 4874	EISM	197.4	24.49	596.4	36.10	4273.3	97.45	87.7
	CARE	159.7	22.70	128.0	2.86	4527.1	160.95	92.9
	$O\neg I$	168.3	18.64	60.3	**1.40**	4820.9	78.02	98.9
	$O\neg M$	137.2	11.95	486.2	19.60	4339.3	151.56	89.0
	Proposed	**128.4**	**4.27**	**55.0**	1.51	**4865.6**	**6.99**	**99.8**
Indoor 73×53 24375	EISM	601.6	79.70	510.6	26.41	21921.4	677.91	89.9
	CARE	442.8	37.43	170.3	10.63	23557.0	182.92	96.6
	$O\neg I$	565.9	35.19	70.2	5.86	24131.3	96.75	99.0
	$O\neg M$	440.3	29.82	452.2	18.01	21864.4	198.76	89.7
	Proposed	**404.8**	**18.29**	**63.0**	**5.70**	**24319.0**	**30.46**	**99.8**
Lab 70×70 21750	EISM	730.7	75.75	450.1	39.00	19979.1	720.65	91.9
	CARE	702.0	83.83	151.8	**3.90**	21102.3	390.62	97.0
	$O\neg I$	715.4	32.72	77.4	15.23	21489.0	335.71	98.8
	$O\neg M$	608.3	25.71	372.4	33.11	20118.8	564.92	92.5
	Proposed	**580.4**	**9.71**	**69.8**	10.10	**21585.0**	**205.09**	**99.2**

[1]Max entropy: the maximum map entropy that can be reduced theoretically (considering inflate range).
[2]Algorithm runtime: the calculation time cost per planning period.
[3]Coverage rate: the ratio of actual entropy change to maximum map entropy when exploration stops.
*: ↑ higher is better. ↓: lower is better.

simulations run on an AMD R9-7940HX CPU and 32 GB of RAM with ROS1 on Ubuntu 20.04 system.

A. Simulation Experiments

To evaluate the exploration performance, simulations are conducted in three scenes with increasing complexity and size, as shown in Fig. 4, named "Maze", "Indoor" and "Lab".

- *Maze:* Derived from [9]. A small-scale structured scene with small corners.
- *Indoor:* The scope is larger than Maze, and additional modifications are made by introducing intersections and compact rooms to simulate more complex scenes.
- *Lab:* The prototype is the Intel Lab from 2D dataset [25]. We build an equal scale 3D scene in Gazebo. The environment features multiple doorways, unstructured obstacles and narrow passages.

We split the simulation tests into a horizontal comparison with information gain-based approaches, and a vertical comparison with other state-of-the-art (SOTA) types of exploration methods. Each method is executed 10 times under identical initial configuration. Some common parameter settings are summarized in Table I. Tables II and III record statistic results of different methods, including exploration time, key metrics and coverage rate. Note that the key metrics vary depending on experimental focus, as discussed below.

1) Test 1: We first compared our method with two previous information gain-based methods, EISM [19] and CARE [7], as

TABLE III
STATISTIC RESULTS OF TEST 2 OVER 10 RUNS

Scene / Size(m^2) / Max area[1] (m^2)	Method	Exploration time(s)↓		Movement distance(m)↓		Explored area(m^2)↑		Coverage rate[2](%)↑
		Avg	*Std*	*Avg*	*Std*	*Avg*	*Std*	*Avg*
Maze 35×24 780	TARE	145.3	19.03	209.5	22.18	776.5	9.02	99.6
	FAEL	155.5	29.66	155.4	7.51	734.3	9.00	94.1
	HPHS	132.6	10.24	147.7	10.15	764.1	**1.80**	97.9
	Proposed	**129.1**	**10.07**	**139.5**	**5.08**	**778.9**	3.16	**99.9**
Indoor 73×53 3900	TARE	605.9	73.78	907.2	82.86	3880.1	14.06	99.5
	FAEL	474.3	30.19	627.7	**21.06**	3808.2	**1.83**	97.7
	HPHS	718.3	81.05	720.6	70.53	3747.6	38.94	96.1
	Proposed	**414.1**	**23.13**	**520.6**	29.61	**3891.0**	4.87	**99.8**
Lab 70×70 3480	TARE	817.7	106.72	1188.7	160.47	3429.9	104.55	98.6
	FAEL	623.3	92.20	741.0	89.99	3332.0	138.59	95.7
	HPHS	999.4	95.04	994.0	98.27	3368.3	66.59	96.8
	Proposed	**582.2**	**18.69**	**702.8**	**18.70**	**3453.6**	**32.82**	**99.2**

[1]Max area: the maximum area that can be observed theoretically (considering inflate range).
[2]Coverage rate: the ratio of actual entropy change to maximum entropy when exploration stops.

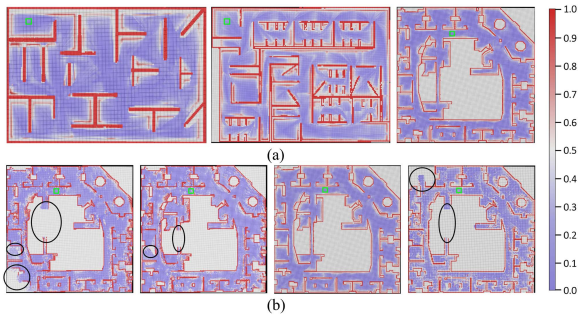

Fig. 5. Constructed 2D-OGMs, where green hollow squares are start points and black ovals are missing regions. (a) Maze, Indoor and Lab by Proposed method. (b) Lab, from left to right: EISM, CARE, $O\neg I$, $O\neg M$.

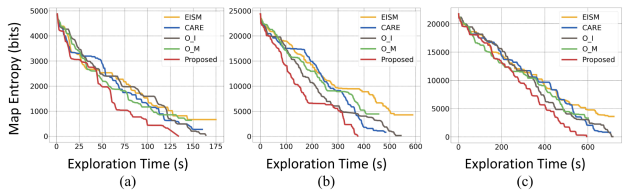

Fig. 6. T-ME curves of each scene. (a) Maze. (b) Indoor. (c) Lab.

well as two ablation studies, ours without IRSR ($O\neg I$) and ours without MTSM ($(O\neg M$, using ISM instead) considering two main metrics: algorithm runtime and map entropy, to evaluate the superiority of our sensor model and real-time performance. EISM updates map occupancy based on exact ISM and uses 8-axis raycasting for full action evaluation. CARE is developed on SCM and determines the optimal target by BKIO, where the initial training pool is composed of 30 randomly selected voxels. The 2D-OGMs constructed by our method in all three scenarios are presented in Fig. 5(a), while the results of comparative schemes in the **Lab** are shown in Fig. 5(b). Fig. 6 illustrates the curves of map entropy change over time (T-ME), where subfigure (c) corresponds to the results of **Lab** in Fig. 5.

It can be seen that EISM exhibits more entropy reduction in the early stage compared to CARE (e.g., the first 50 s in the **Maze** and first 200 s in the **Indoor**) due to naive ISM. However, its final map entropy changes cannot reach the maximum. CARE, on the other hand, yields smoother entropy transitions and higher overall map entropy reduction than EISM, but its SCM still limits complete coverage. In contrast, the proposed method achieves both rapid and complete entropy reduction across all three scenarios. Specifically, the statistic results in Table II show that our method improves 2.3%∼7.5% and 7.9%∼13.8% in map entropy reduction than EISM and CARE, and is the only method that achieves an overall coverage rate exceeding

Authorized licensed use limited to: Southeast University. Downloaded on November 04,2025 at 02:29:11 UTC from IEEE Xplore. Restrictions apply.

IEEE Robotics and Automation Letters (RA-L) paper, presented at ICRA 2026, Vienna, Austria. Cite as RA-L paper.

99% across three scenes. This improvement stems from MTSM that ensures consistent exploration of all narrow regions in 10 trials, whereas EISM always misses compact rooms and notably fails to pass through the narrow passage in the **Lab** in all experiments. CARE sporadically explores the narrow passage but still overlooks small corners in each scene, as illustrated in Fig. 5(b). In addition, the proposed method significantly reduces algorithm runtime by 84.5%∼90.8% compared to EISM and 54.0%∼63.0% compared to CARE. These results highlight that the optimized BKIO greatly accelerates optimal target determination.

In the ablation studies, $O\neg I$ successfully explores all narrow regions, maintaining map entropy reduction and algorithm runtime at levels comparable to the full method. However, due to the lack of global heuristic guidance, it exhibits significantly longer exploration time, which is 18.9%∼28.5% longer than the Proposed. $O\neg M$, on the other hand, achieves faster overall exploration since global planning reduces some local re-planning cycles, but it misses details in narrow regions, resulting in overall map entropy reduction 7.3%∼12.1% lower than the Proposed. These results demonstrate the contributions of proposed modules in our framework: MTSM enhances information acquisition in narrow regions, while IRSR provides global dead-zone guidance, together ensuring robust and efficient exploration.

2) Test 2: To further validate the performance of our framework against the other two paradigms in terms of exploration efficiency and environmental coverage, we chose the sampling-based method TARE [4], Frontier-based method FAEL [6], and hybrid method HPHS [9] as comparative schemes, considering movement distance and explored area as key metrics. TARE is a pioneering approach combining local uniform sampling and global fast traversal. FAEL is a fast exploration framework designed for large environment, which adopts the idea of Frontier and roadmap. HPHS is a hierarchical planning method that adopts hybrid Frontier sampling at the point cloud level. In addition to the common settings listed in Table I, other parameters of the compared methods were kept the same as those in the references. The representative trajectories and curves of explored volume over distance (D-EV) are presented in Fig. 7.

The results show that our method completes exploration first in all scenes with minimal redundant paths. Even in **Indoor** and **Lab** scenarios featuring narrow passages and multiple small rooms, it achieves efficient sequential coverage. The integration of MTSM strengthens the system's focus on narrow regions, minimizing omissions of critical details. In contrast, TARE, FAEL and HPHS all prioritize open areas at the beginning phase (e.g., the first 200 s in the **Indoor**), and all pass through narrow passages in the **Lab**. Nevertheless, FAEL experiences extensive backtracking due to incomplete exploration of narrow regions on the first pass. TARE occasionally gets trapped in dead zones and struggles to escape. HPHS performs poorly in environments with compact rooms and small corners due to insufficient accuracy of point-cloud-level processing, and the similar cost of subregions often leads to back-and-forth movements. These situations reflect in the slow growth of D-EV curves in the latter stage of exploration, leading to reduced efficiency.

The data presented in Table III indicate that our method achieves broader scene coverage with less time cost and shorter path length. Compared with TARE, our approach achieves a basic consistent coverage rate level over 99%, but the exploration time is reduced by 11.1%∼31.7% and the movement distance is significantly shortened by 33.4%∼42.6%. In comparison with FAEL, our method reduces time and distance by 6.6%∼17.0%

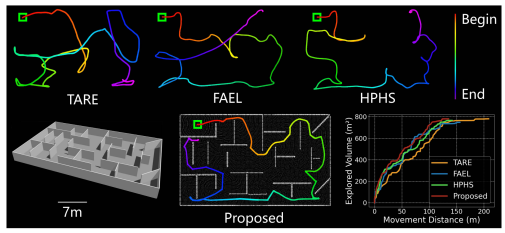

(a)

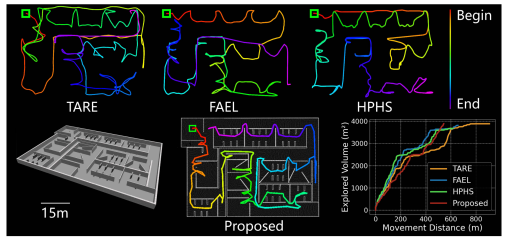

(b)

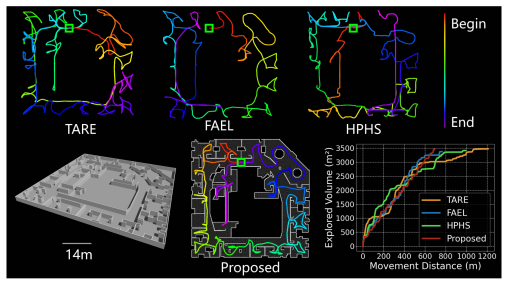

(c)

Fig. 7. Simulation results, where the green hollow square is the start point and the rainbow line is the trajectory. (a) Maze. (b) Indoor. (c) Lab.

and 4.9∼17.1%, and improves the coverage rate by 2.1%∼6.2% as FAEL leaves several unexplored areas in big scenes. When compared to HPHS, the exploration time and movement distance are reduced by 2.6%∼42.3% and 5.6%∼29.3%, while the coverage rate is enhanced by 2.0%∼3.9%, as HPHS exhibits more redundant paths and leaves unexplored areas in complex environments. The synergy between improved sensor model and global guidance of our method greatly enhances overall exploration efficiency.

B. Real-World Experiment

A custom-built differential chassis serves as the AGV platform, which is equipped with an Intel NUC13VYKI5 (with an Intel i5–1340P CPU and 16 GB of RAM), a MTI–30 IMU and a RS–32–LiDAR. The real experiment is conducted in an indoor environment with intersections, narrow passages and obstacles (Fig. 8), where minimal manual interventions are introduced in slope and stair areas out of precaution. An in-house modified version of Fastlio2 [26] is employed as the SLAM module to both acquire AGV location and mapping. The parameters are consistent with those listed in Table I, except that the velocity v is limited to 0.6 m/s to ensure safety during exploration, and the resolution of 2D-OGM is set to 0.2 m to explore finer environmental details.

Fig. 8 shows the constructed point cloud map, 2D-OGM and trajectory. The AGV explores 2918.4m^2 and reduces the map entropy by 72960bits over 439.4 s and 165.1 m. The results shows that our proposed framework is capable to efficiently exploring a real complex environment with narrow regions through

Authorized licensed use limited to: Southeast University. Downloaded on November 04,2025 at 02:29:11 UTC from IEEE Xplore. Restrictions apply.

IEEE Robotics and Automation Letters (RA-L) paper, presented at ICRA 2026, Vienna, Austria. Cite as RA-L paper.

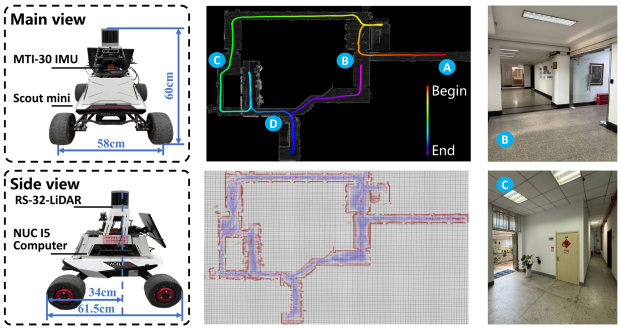

Fig. 8. The real-world experiment. **Left**: AGV platfrom. **Mid**: The exploration trajectory and 2D-OGM, where the occupied voxels appearing in the free area are experimental personnel following the AGV during the experimental process. **Right**: Corresponding real scenes, where B and D are intersections, A and C are narrow passages.

an actual AGV platform. For more real-world comparisons, please refer to our demonstration video[2].

VI. Conclusion

In this letter, a tiered framework is proposed for efficient AGV autonomous exploration in complex environments featuring narrow regions. A novel sensor model is introduced to enhance the acquisition of environmental information, and the Frontier set is defined from a probabilistic distribution perspective to accelerate the convergence of Bayesian optimization for optimal local target determination. Besides, an informative sparse roadmap is designed using the accumulated historical knowledge during the exploration process, and the global heuristic guidance is realized by solving an ATSP based on the roadmap in dead zone scenarios. Simulation results demonstrate that our approach achieves faster algorithm runtime and more comprehensive information acquisition compared to existing information gain-based methods, as well as outperforms other SOTA approaches in terms of exploration efficiency and environment coverage. Real-world experiments further validate the strong potential of our method for practical engineering applications.

Our work has the potential to be extended to 3D scenes, while more complex environmental structures and larger voxel counts pose greater challenges for accurate information evaluation and real-time performance. Future work will explore 3D Gaussian Splatting for continuous spatial representation and reinforcement learning for the optimal targe determination.

References

[1] Z. Shiyong, Z. Xuebo, D. Qianli, W. Ziyu, X. Haobo, and Y. Jing, "FSMP: A frontier-sampling-mixed planner for fast autonomous exploration of complex and large 3D environments," *IEEE Trans. Instrum. Meas*, vol. 74, Mar. 2025.

[2] Z. Yichen, C. Xinyi, F. Chen, Z. Boyu, and S. Shaojie, "FALCON: Fast autonomous aerial exploration using coverage path guidance," *IEEE Trans. Robot.*, vol. 41, pp. 1365–1385, Feb. 2025.

[3] G. Shuang, N. Zelin, Z. Fu, and Z. Boyu, "EPIC: A lightweight LiDAR-based AAV exploration framework for large-scale scenarios," *IEEE Robot. Automat. Lett.*, vol. 10, no. 5, pp. 5090–5097, May 2025.

[4] C. Chao, Z. Hongbiao, C. Howie, and Z. Ji, "TARE: A hierarchical framework for efficiently exploring complex 3D environments," *Robot.: Sci. Syst.*, vol. 5, pp. 136–144, Jan. 2021.

[5] Z. Huazhang, L. Tian, M. Shunzheng, Z. Xuan, S. Huiliang, and L. Ruijiao, "CODE: Complete coverage AAV exploration planner using dual-type viewpoints for multi-layer complex environments," *IEEE Robot. Automat. Lett.*, vol. 10, no. 2, pp. 1880–1887, Feb. 2025.

[6] H. Junlong et al., "FAEL: Fast autonomous exploration for large-scale environments with a mobile robot," *IEEE Robot. Automat. Lett.*, vol. 8, no. 3, pp. 1667–1674, Mar. 2023.

[7] X. Yang, Z. Ronghao, Z. Senlin, L. Meiqin, and H. Shoudong, "CARE: Confidence-rich autonomous robot exploration using Bayesian kernel inference and optimization," *IEEE Robot. Automat. Lett.*, vol. 8, no. 10, pp. 6755–6762, Oct. 2023.

[8] B. Yamauchi, "A Frontier-based approach for autonomous exploration," in *Proc. IEEE Int. Symp. Comput. Intell. Robot. Automat. CIRA'97. New Comput. Princ. Robot. Automat.*, 1997, pp. 146–151.

[9] L. Shijun, L. Ying, W. Chenming, X. Bin, and F. Wei, "HPHS: Hierarchical planning based on hybrid frontier sampling for unknown environments exploration," in *Proc. IEEE/RSJ Int. Conf. Intell. Robots Syst.*, 2024, pp. 12056–12063.

[10] Z. Boyu, Z. Yichen, C. Xinyi, and S. Shaojie, "FUEL: Fast UAV exploration using incremental Frontier structure and hierarchical planning," *IEEE Robot. Automat. Lett.*, vol. 6, no. 2, pp. 779–786, Apr. 2021.

[11] B. Andreas, K. Mina, A. Kostas, O. Helen, and S. Roland, "Receding horizon "Next–Best–View" planner for 3D exploration," in *Proc. IEEE Int. Conf. Robot. Autom.*, 2016, pp. 1462–1468.

[12] W. Christian, F. Marius, B. Rik, O. Helen, and S. Roland, "History-aware autonomous exploration in confined environments using mavs," in *Proc. IEEE/RSJ Int. Conf. Intell. Robots Syst.*, 2018, pp. 5208–5215.

[13] T. Dang, M. Frank, K. Shehryar, P. Christos, and A. Kostas, "Graph-based path planning for autonomous robotic exploration in subterranean environments," in *Proc. IEEE/RSJ Int. Conf. Intell. Robots Syst.*, 2019, pp. 3105–3112.

[14] X. Zhefan, D. Di, and S. Kenji, "Autonomous UAV exploration of dynamic environments via incremental sampling and probabilistic roadmap," *IEEE Robot. Automat. Lett.*, vol. 6, no. 2, pp. 2729–2736, Apr. 2021.

[15] J. Maani, Ghaffari, M. Jaime, Valls, and D. Gamini, "Sampling-based incremental information gathering with applications to robotic exploration and environmental monitoring," *Int. J. Robot. Res.*, vol. 38, no. 6, pp. 658–685, May 2019.

[16] X. Yang, Z. Ronghao, Z. Senlin, L. Meiqin, and Y. Junzhi, "Uncertainty-aware autonomous robot exploration using confidence-rich localization and mapping," *IEEE Trans. Autom. Sci. Eng.*, vol. 22, pp. 1124–1138, Feb. 2025.

[17] K. Evan, L. Taeyoung, A. Zhuming, and M. Iras, "Bayesian occupancy grid mapping via an exact inverse sensor model," in *Proc. Amer. Control Conf.,* 2016, pp. 5709–5715.

[18] K. Evan, L. Taeyoung, and A. Zhuming, "Autonomous exploration by expected information gain from probabilistic occupancy grid mapping," in *Proc. IEEE Int. Conf. Simul., Model. Program. Auto. Robot.,* 2016, pp. 246–251.

[19] K. Evan, T. Kuya, L. Taeyoung, and A. Zhuming, "Autonomous exploration with exact inverse sensor models," *J. Intell. Robot. Syst.*, vol. 92, no. 3, pp. 435–452, Dec. 2018.

[20] A. Ali-akbar, H. Eric, H. Karol, and S. Gaurav, "Confidence-rich grid mapping," *Int. J. Robot. Res.*, vol. 38, no. 5, pp. 1–23, May 2019.

[21] X. Yang, Z. Ronghao, L. Meiqin, and Z. Senlin, "CRMI: Confidence-rich mutual information for information-theoretic mapping," *IEEE Robot. Automat. Lett.*, vol. 6, no. 4, pp. 6434–6441, Oct. 2021.

[22] B. Shi, W. Jinkun, C. Fanfei, and E. Brendan, "Information-theoretic exploration with Bayesian optimization," in *Proc. IEEE/RSJ Int. Conf. Intell. Robots Syst.*, 2016, pp. 1816–1822.

[23] J. Maani, Ghaffari, M. Jaime, Valls, and D. Gamini, "Gaussian processes autonomous mapping and exploration for range-sensing mobile robots," *Auton. Robot.*, vol. 42, no. 2, pp. 273–290, Feb. 2018.

[24] M. Roman and R. Fabio, "Bayesian optimisation for intelligent environmental monitoring," in *Proc. IEEE/RSJ Intl. Conf. Intell. Robots Syst.*, 2012, pp. 2242–2249.

[25] H. Andrew and R. Nicholas, "The robotics data set repository (Radish)," 2014, Stachniss Lab. [Online]. Available: http://www2.informatik.uni-freiburg.de/stachnis/datasets.html

[26] X. Wei, C. Yixi, H. Dongjiao, L. Jiarong, and F. Zhang, "FAST-LIO2: Fast direct LiDAR-inertial odometry," *IEEE Trans. Robot.*, vol. 38, no. 4, pp. 2053–2073, Aug. 2022.

[2]https://youtu.be/0_vi6ks_7sw

Authorized licensed use limited to: Southeast University. Downloaded on November 04,2025 at 02:29:11 UTC from IEEE Xplore. Restrictions apply.